Ultrasonics 98 (2019) 20–27

Contents lists available at ScienceDirect

Ultrasonics

journal homepage: www.elsevier.com/locate/ultras

Enhanced ultrasonic detection of near-surface flaws using transverse-wave backscatter

Yuantian Huang[a], Joseph A. Turner[b], Yongfeng Song[a], Peijun Ni[c], Xiongbing Li[a,d,*]

[a] School of Traffic and Transportation Engineering, Central South University, Changsha 410075, China
[b] Mechanical and Materials Engineering, University of Nebraska-Lincoln, Lincoln, NE 68588, USA
[c] Inner Mongolia Metallic Materials Research Institute, Ningbo 315103, China
[d] Key Laboratory of Traffic Safety on Track (Central South University), Ministry of Education, Changsha 410075, China

ARTICLE INFO

Keywords:
Ultrasonic testing
Transverse-to-transverse (T-T) scattering
Time-dependent threshold
Sub-wavelength near-surface flaws
Grain size distribution
Extreme value statistics

ABSTRACT

Diffuse ultrasonic backscatter measurements have been shown to enhance the detection capability of sub-wavelength flaws when combined with extreme value statistics. However, for a normal-incidence immersion measurement, a "dead zone" created by the ring-down of the front-wall echo will hide near-surface flaws. In this article, a pulse-echo transverse wave backscatter measurement is used to detect near-surface flaws under high gain. The approach is validated using a magnesium specimen with side-drilled holes. The confidence bounds of the grain noise from this specimen are given by a transverse-to-transverse scattering model, which takes the grain size distribution and the hexagonal crystal symmetry into account. The upper bound is then treated as a time-dependent threshold for the C-scan. Experiments show that the developed method has good performance for detecting sub-wavelength, near-surface flaws, and can suppress both missed detections and false positives.

1. Introduction

Near-surface flaws, such as forging cracks, fatigue cracks and stress corrosion cracks, are very harmful to component structural health [1]. When these flaws reach a critical size, they can lead to structural failure [1]. Ultrasonic detection techniques are used widely to detect flaws in materials [2]. However, in normal-incidence immersion measurements the flaw echoes can be hidden in the dead zone caused by the front-wall echoes [3]. During the past two decades, researchers have tried some digital signal processing techniques to separate flaw echoes from front-wall echoes, such as cepstrum analysis [4], Hilbert transform [5], deconvolution algorithms [6,7], pulse compression techniques [8] and time-domain phase analysis method [3]. However, these methods require a strict linearity of the signals and can only detect flaws larger than the wavelength. Surface or Rayleigh wave methods can be used to interrogate flaws near surfaces. However, most of the energy of a surface wave propagates at a depth equal to the wavelength (~0.6 mm at 5 MHz in magnesium alloy) [9]. When flaws are located deeper than the penetration depth, surface wave methods will break down. Otherwise, lower frequencies are necessary to inspect any substantial depth, which adversely affects detectability of small defects [10].

Due to an oblique-incidence transducer configuration using mode-converted transverse waves can eliminate front-wall echoes in the measured signal, which would allow inspection depths closer to the surface [11]. However, if the flaw size is smaller than the wavelength of the ultrasound applied in the detection, flaw echoes are often masked by the ultrasonic scattering (or grain noise) from the heterogeneous background [12]. Therefore, detecting sub-wavelength near-surface flaws in materials is still a challenge in current ultrasonic non-destructive evaluation. Recently, Song et al. [13,14] proposed an ultra-high gain detection method based on ultrasonic backscatter [12] and extreme value statistical theory [15]. Instead of using a fixed threshold, a time-dependent threshold is used to detect sub-wavelength flaws in a 304 stainless steel specimen [13]. Their method can significantly reduce the false detection and missed detection rates of sub-wavelength flaws. However, because their method uses a normal-incidence immersion configuration, it cannot be adopted for the detection of near-surface flaws.

In this article, the aim is to detect near-surface, sub-wavelength, side-drilled holes in a magnesium alloy specimen. First, the transverse-to-transverse (T-T) scattering model [16] is modified to include the grain size distribution and hexagonal crystal symmetry appropriate for the magnesium alloy of interest. Secondly, the modified model is employed with extreme value statistics to extend Song's method [13] from the normal-incidence case to the oblique-incidence case. Finally, we use the present method to explore the detection of sub-wavelength flaws

* Corresponding author at: School of Traffic and Transportation Engineering, Central South University, Changsha 410075, China.
E-mail address: lixb_ex@163.com (X. Li).

https://doi.org/10.1016/j.ultras.2019.05.010
Received 4 January 2019; Received in revised form 8 May 2019; Accepted 27 May 2019
Available online 28 May 2019

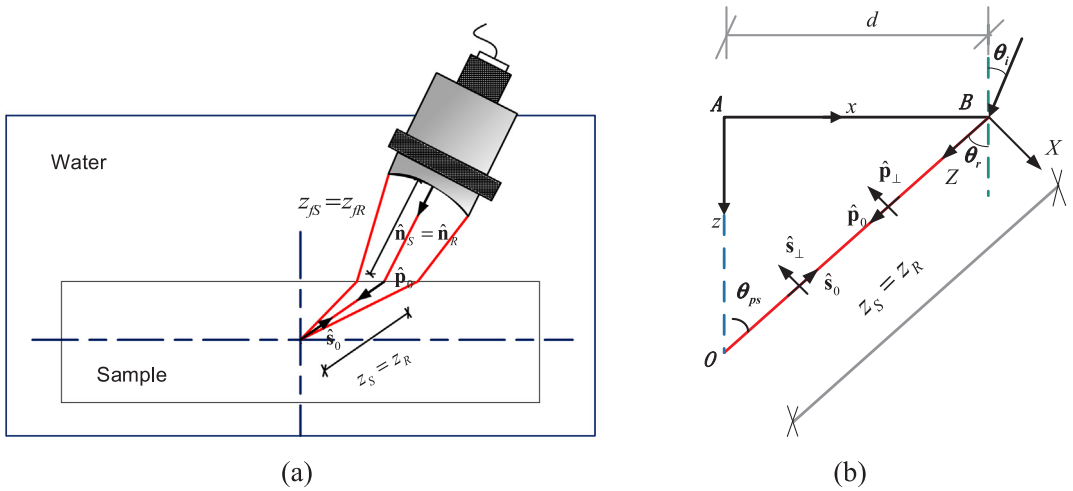

Fig. 1. Schematic diagram of the T-T mode-converted ultrasonic scattering model (a) the pulse-echo transducer configuration, (b) The geometrical coordinate transformation.

near the surface of a magnesium alloy.

2. Theory

Hu et al. [16] derived a T-T scattering model for the ultrasonic transducer configuration shown in Fig. 1(a). The spatial variance of the T-T response can be written as

$$\Phi_{\mathrm{TT}}^{\mathrm{PE}}(t)=\Phi_{TT}^{0}(\theta_i,\theta_r)\{\tilde{\eta}_{TT}(\pi)\Xi_{\cdots\hat{\mathbf{p}}_\perp\hat{\mathbf{p}}_0\hat{\mathbf{s}}_0\hat{\mathbf{s}}_\perp}^{\cdots\hat{\mathbf{p}}_\perp\hat{\mathbf{p}}_0\hat{\mathbf{s}}_0\hat{\mathbf{s}}_\perp}(\pi)\}\psi_{TT}(X,Y,Z,t)\,, \tag{1}$$

where the subscript TT in $\Phi_{\mathrm{PE}}^{\mathrm{TT}}(t)$ is used to denote transverse-to-transverse (T-T) scattering, and the super script PE represents the pulse-echo transducer configuration, which assumes the sound fields of the source and receiver are the same. The parameter Φ_{TT}^{0} is a constant related to the experiment calibration, and ψ_{TT} is the field distribution function describing the transducer beam and the input pulse. As shown in Fig. 1(b), θ_i and θ_r represent the angle of incidence and the angle of refraction, respectively. **x** defines the global coordinate, and **X** defines the local coordinate. The local coordinate can be converted into the global coordinate using the coordinate transformations [16]

$$\begin{cases} X=x\cos\theta_r+z\sin\theta_r-d\cos\theta_r\,, \\ Y=y\,, \\ Z=-x\sin\theta_r+z\cos\theta_r+d\sin\theta_r\,, \end{cases} \tag{2}$$

where d is the offset distance. Note that the material path of the source z_S equals the material path of the receiver z_R.

The quantity $\tilde{\eta}_{TT}(\pi)\Xi_{\cdots\hat{\mathbf{p}}_\perp\hat{\mathbf{p}}_0\hat{\mathbf{s}}_0\hat{\mathbf{s}}_\perp}^{\cdots\hat{\mathbf{p}}_\perp\hat{\mathbf{p}}_0\hat{\mathbf{s}}_0\hat{\mathbf{s}}_\perp}(\pi)$ in Eq. (1) is known as the transverse-to-transverse diffuse backscatter coefficient, which is used to characterize the microstructural properties. It includes a correlation function $\tilde{\eta}$ and a covariance function Ξ. In this work, we will focus on the modification of the scattering coefficient for magnesium alloys containing equiaxed single-phase grains with hexagonal crystal symmetry and grain size distribution.

The term $\Xi_{\cdots\hat{\mathbf{p}}_\perp\hat{\mathbf{p}}_0\hat{\mathbf{s}}_0\hat{\mathbf{s}}_\perp}^{\cdots\hat{\mathbf{p}}_\perp\hat{\mathbf{p}}_0\hat{\mathbf{s}}_0\hat{\mathbf{s}}_\perp}(\pi)$ is the inner product on the eighth-rank covariance tensor defined as

$$\Xi_{\cdots\hat{\mathbf{p}}_\perp\hat{\mathbf{p}}_0\hat{\mathbf{s}}_0\hat{\mathbf{s}}_\perp}^{\cdots\hat{\mathbf{p}}_\perp\hat{\mathbf{p}}_0\hat{\mathbf{s}}_0\hat{\mathbf{s}}_\perp}(\theta_{ps})=\Xi_{lmjk}^{\alpha\delta\beta\gamma}\hat{p}_{\perp\gamma}\hat{p}_{\perp k}\hat{s}_{\perp\beta}\hat{s}_{\perp j}\hat{p}_{0\delta}\hat{p}_{0m}\hat{s}_{0\alpha}\hat{s}_{0l}\,, \tag{3}$$

where $\Xi_{lmjk}^{\alpha\delta\beta\gamma}=\langle C_{ijkl}C_{\alpha\beta\gamma\delta}\rangle-\langle C_{ijkl}\rangle\langle C_{\alpha\beta\gamma\delta}\rangle$. C_{ijkl} is the fourth-rank elastic modulus tensor (the angular brackets $\langle\ \rangle$ indicate an ensemble average) and θ_{ps} is the angle between the incident and scattered waves in the material. It can be reduced for the case of hexagonal crystal symmetry. Assuming Voigt averaging of the elastic moduli and using the transducer configuration given in Fig. 1(a) gives [17,18,19]

$$\Xi_{\cdots\hat{\mathbf{p}}_\perp\hat{\mathbf{p}}_0\hat{\mathbf{s}}_0\hat{\mathbf{s}}_\perp}^{\cdots\hat{\mathbf{p}}_\perp\hat{\mathbf{p}}_0\hat{\mathbf{s}}_0\hat{\mathbf{s}}_\perp}(\theta_{ps})=\frac{1}{6300}(A_0+A_1\cos 2\theta_{ps}+A_2\cos^2 2\theta_{ps})\,, \tag{4}$$

where the coefficients A_0, A_1, and A_2 are combinations of single crystal elastic constants c_{11}, c_{12}, c_{13}, c_{33}, c_{44}. The coefficients of the inner products are found to be

$$\begin{cases} A_0=55c_{11}^2+315c_{12}^2+220c_{13}^2+20c_{33}^2+460c_{44}^2-210c_{11}c_{12} \\ \quad +60c_{11}c_{13}-420c_{12}c_{13}+40c_{11}c_{33}-80c_{13}c_{33}-300c_{11}c_{44} \\ \quad +420c_{12}c_{44}+40c_{13}c_{44}-160c_{33}c_{44}\,, \\ A_1=-30c_{11}^2+210c_{12}^2+120c_{13}^2+40c_{44}^2+20c_{11}c_{12}-320c_{12}c_{13} \\ \quad +40c_{11}c_{33}-120c_{12}c_{33}+80c_{13}c_{33}+40c_{11}c_{44}+200c_{12}c_{44} \\ \quad -160c_{13}c_{44}-80c_{33}c_{44}\,, \\ A_2=7c_{11}^2+35c_{12}^2+28c_{13}^2+12c_{33}^2+12c_{44}^2+30c_{11}c_{12}-28c_{11}c_{13} \\ \quad -60c_{12}c_{13}-16c_{11}c_{33}-40c_{12}c_{33}+32c_{13}c_{33}+4c_{11}c_{44} \\ \quad +20c_{12}c_{44}-8c_{13}c_{44}-16c_{33}c_{44}\,. \end{cases} \tag{5}$$

Here, $\tilde{\eta}$ is the spatial Fourier transform of the corresponding two-point correlation function $\eta(|\mathbf{r}-\mathbf{r}'|)$, which describes the probability that two randomly chosen points $\mathbf{r}$ and $\mathbf{r}'$ lie within the same grain [20,21]. Considering the grain size distribution present in the magnesium alloy, the spatial correlation function $\tilde{\eta}$ must be modified accordingly. A log-normal distribution of a variable L is defined so that the variable $x=\ln L$ follows a normal distribution with mean μ and standard deviation σ_d. The log-normal grain volume distribution can then be written as [22]

$$P(L)=\frac{1}{L\sigma_d\sqrt{2\pi}}\exp\left[-\frac{\ln^2(L/\widetilde{L})}{2\sigma_d^2}\right], \tag{6}$$

where $\widetilde{L}$ is the median of the distribution given by $\widetilde{L}=\exp\mu$, which is related to the mean by $\bar{L}=\widetilde{L}\exp(\sigma_d^2/2)$. Hence, for a continuous distribution of grain size, the spatial correlation function can be written as [22]

$$\eta(r)=\int_0^\infty P(L)\exp(-r/L)dL\,. \tag{7}$$

Then the correlation function in transform space for a distribution of grain size is written as [22]

$$\tilde{\eta}_{TL}(\theta_{ps})=\tilde{\eta}(\mathbf{s}-\mathbf{p})=\frac{1}{2\pi^3}\int_0^\infty d\mathbf{r}\tilde{\eta}(\mathbf{r})\exp[-i(\mathbf{s}-\mathbf{p})\cdot\mathbf{r}]$$

$$=\int_0^\infty P(L)\frac{L^3}{\pi^2[1+L^2(k_L^2+k_T^2+2k_Lk_T\cos\theta_{ps})]}dL\quad, \tag{8}$$

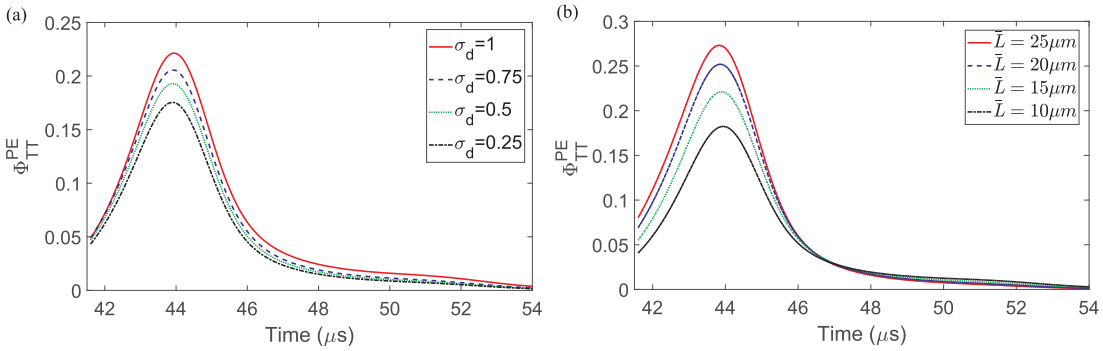

Fig. 2. Effect of grain size distributions on theoretical variance curves. (a) Different distributions σ_d with the same mean $\bar{L}$ = 13.5 μm, (b) different mean grain size $\bar{L}$ with the same σ_d = 0.75.

$$\widetilde{\eta}_{TT}(\theta_{ps}) = \widetilde{\eta}(\mathbf{s}-\mathbf{p}) = \frac{1}{2\pi^3}\int_0^\infty d\mathbf{r}\widetilde{\eta}(\mathbf{r})\exp[-i(\mathbf{s}-\mathbf{p})\cdot\mathbf{r}]$$

$$= \int_0^\infty P(L)\frac{L^3}{\pi^2[1+2k_T^2L^2(1+\cos\theta_{ps})]}dL \quad , \tag{9}$$

where $k_L = \omega_0/c_L$ is the longitudinal wave number in the specimen, and $k_T = \omega_0/c_T$ is the transverse wave number in the specimen, and $\omega_0 = 2\pi f_0$ is the angular center frequency. The modified backscatter coefficient is substituted into Eq. (1). The transverse attenuation coefficient α_T of the ultrasonic wave in the material is also related to the $\widetilde{\eta}$ and Ξ. The expression for α_T is included in the Appendix A. It should be noted that the Voigt average is used to estimate the wave velocity of the solid. Thus, with the Voigt average, the longitudinal velocity c_L and transverse wave velocity c_T can be also derived from C_{ijkl} [23,24]

$$\begin{cases} c_L = \sqrt{\langle C_{1111}\rangle/\rho}\ , \\ c_T = \sqrt{\langle C_{2323}\rangle/\rho}\ , \end{cases} \tag{10}$$

where ρ is density of the material, and
$\langle C_{1111}\rangle = (8c_{11} + 4c_{13} + 3c_{33} + 8c_{44})/15$,
$\langle C_{2323}\rangle = (7c_{11} - 5c_{12} - 4c_{13} + 2c_{33} + 12c_{44})/30$.

Finally, based on the time-dependent threshold for the L-L model developed by Song et al. [13,14] we can establish the time-dependent threshold for the T-T model with a similar formalism. The maximum possible grain noise amplitude obeys the Gumbel extreme value distribution [15]. Thus, the mathematical expectation of maximum amplitude can be estimated as [13,15]

$$A_{\max}(t) = \frac{\sqrt{\Phi(t)}}{2\sqrt{2\ln N}}\ln\left[\frac{N^4\exp(2\gamma)}{\pi\ln N}\right], \tag{11}$$

where $\gamma \approx 0.5772$ is the Euler-Mascheroni constant, and N is the number of waveforms. According to the quantile function of the Gumbel distribution, the upper and lower confidence bounds associated with $A_{\max}(t)$ can be defined as [13,15]

$$U(t) = \frac{\sqrt{\Phi(t)}}{2\sqrt{2\ln N}}\left\{\ln\left(\frac{N^4}{\pi\ln N}\right) - 2\ln\left[-\ln\left(\frac{1+\alpha}{2}\right)\right]\right\}, \text{ and} \tag{12}$$

$$L(t) = \frac{\sqrt{\Phi(t)}}{2\sqrt{2\ln N}}\left\{\ln\left(\frac{N^4}{\pi\ln N}\right) - 2\ln\left[-\ln\left(\frac{1-\alpha}{2}\right)\right]\right\}, \tag{13}$$

where α is the confidence level. In practice, the upper bound $U^{\text{theory}}(t)$ can be treated as an amplitude threshold to be triggered by an echo caused by a flaw. Consequently, the C-scan image can be segmented with a time-dependent threshold as

$$\widetilde{I}_{(i,j)}^{AMP} = \begin{cases} I_{(i,j)}^{AMP}, \exists\ |V_{(i,j)}(t_0 \leqslant t \leqslant t_{end})| \in [U^{\text{theory}}(t_0 \leqslant t \leqslant t_{end}), \infty] \\ 0 \qquad\qquad , \exists\ |V_{(i,j)}(t_0 \leqslant t \leqslant t_{end})| \in [0, U^{\text{theory}}(t_0 \leqslant t \leqslant t_{end})] \end{cases} \tag{14}$$

where $I_{(i,j)}^{AMP}$ denote the C-scan images of the amplitude before and after segmentation, respectively; i and j denote the row number and column number of a pixel in the C-scan image; t_0 and t_{end} are the beginning and end of the time gate, respectively. In the image $\widetilde{I}_{(i,j)}^{AMP}$, the non-zero values represent the flaws inside the test specimen.

In order to investigate the effect of grain size distribution on the T-T model, numerical calculations are made assuming a magnesium alloy specimen with density of ρ = 1800 kg/m^3, and single crystal elastic constants c_{11} = 64 GPa, c_{12} = 26 GPa, c_{13} = 22 GPa, c_{33} = 67 GPa, c_{44} = 18 GPa [25,26]. Based on Eq. (3), the longitudinal and transverse wave velocities can be estimated as c_L = 5984.7 m/s (0.78\% different from the measured value of 5938.5 m/s), and c_T = 3277.3 m/s (1.31\% different from the measured value of 3234.8 m/s), respectively. Water is used as the couplant, and its density and velocity are assumed as ρ_f = 998 kg/m^3 and c_f = 1486 m/s. The transducers are assumed to have center frequency f_0 = 5 MHz, pulse width σ = 0.57 μs, nominal focal length F = 76.2 mm, element radius a = 12.7 mm. The attenuation coefficients of water and magnesium alloys are α_f = 1.23 Np/m and α_T = 12.36 Np/m at 5 MHz, respectively [27,23]. These parameters correspond with the specimen utilized for the experiments in the next section.

For the following two examples, the angle of incidence of the transducer is $\theta_i = 20°$ (According to Snell's law, the first and second critical angles are $\theta_{\text{I}} = 14.376°$ and $\theta_{\Pi} = 26.963°$, respectively), and the water path is z_f = 30.6 mm. Fig. 2(a) shows the T-T scattering response calculated assuming a constant volumetric mean value of grain size which is kept constant at $\bar{L}$ = 13.5 μm for all distributions. Note that the peak amplitudes increase with wider grain size distributions. Wider distributions include larger grains which have higher scattering. Fig. 2(b) shows the T-T scattering calculated by keeping the distribution width constant at σ_d = 0.75 for different mean grain size $\bar{L}$. Note that peaks increase with the increase of $\bar{L}$. Similarly, larger $\bar{L}$ causes higher backscatter. The results demonstrate that when estimating the grain noise and establishing the time-dependent threshold for sub-wavelength flaws detection, it is necessary to take grain size distribution into account. In the next section, the metallographic testing and ultrasonic experiments are described for the AZ80 magnesium alloy specimen.

3. Experiments

3.1. Specimen preparation

An AZ80 magnesium alloy was used in the experiment to verify the present method. The chemical composition of AZ80 magnesium alloy is shown in Table 1. Two specimens free of flaws were cut from the same original blank. One 10 mm cube specimen (specimen A) was used for metallographic testing, while the other (specimen B, size: 40 mm × 40 mm × 15 mm) was used for ultrasonic experiments. Specimen A was ground by silicon carbide paper down to 2000

Table 1
The chemical composition of AZ80 magnesium alloy.

Element	Al	Zn	Mn	Si	Fe	Cu	Ni	Mg
wt%	8.0–9.0	0.2–0.8	0.1–0.4	< 0.1	< 0.01	< 0.05	< 0.005	Balance

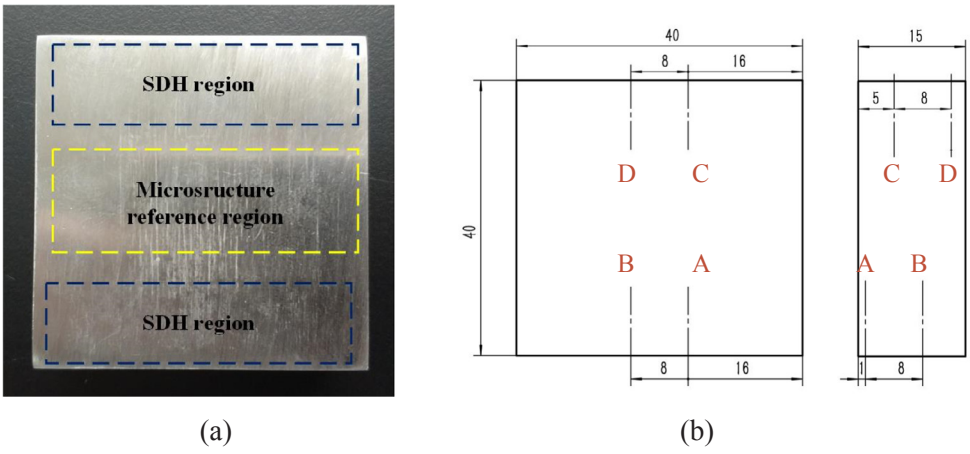

Fig. 3. Schematic diagram of the specimen B (a) specifics of the referenced region and the SDH region, (b) schematic of the artificial SDH specimen.

Table 2
The specifications of artificial SDHs.

SDH	Diameters (mm)	Length (mm)	Buried depth (mm)
A	0.2	10.0	1.0 (in dead zone)
B	0.2	10.0	9.0
C	0.2	10.0	5.0
D	0.2	10.0	13.0

grit, and then fine polished with diamond slurries (particle size 6 and 3 μm) and aluminium oxide slurries (particle size 0.3 and 0.04 μm). Specimen B was ground by sandpapers of 400, 600, and 800 grit. Three regions, i.e. a microstructure reference region and two side-drilled holes (SDH) regions, were designed for specimen B as shown in Fig. 3. Four SDHs with diameter of 0.2 mm were manufactured in the SDH region as specified in Table 2. Compared with the transverse wavelength $\lambda_T = 0.655$ mm (a transducer of 5 MHz), the size of the SDHs is only $0.305\lambda_T$; Hence, they can be treated as sub-wavelength flaws.

3.2. Metallographic analysis

Metallography was conducted to obtain the grain size distribution of the specimen. Specimen A was etched for five seconds. using a solution of 5.5 g $C_6H_2OH(NO_2)_3$ + 2 ml CH_3COOH + 90 ml C_2H_6O + 10 ml H_2O. The metallographic images of the specimen were obtained using an Olympus BX53M microscope system. A total of 50 images were used to obtain the grain size distribution and a representative result is shown in Fig. 4(a). It is noted that $\bar{L} = 1.5\ \bar{l}$, where $\bar{L}$ is the mean three-dimensional grain radius and $\bar{l}$ is the mean two-dimensional grain radius according to Eq. (A2.9) of ASTM standard E112. Fig. 4(b) shows the grain size distribution and the fit based on a log-normal distribution. From the analysis, we find $\bar{L} = 13.4 \pm 0.2\ \mu$m and $\sigma_d = 0.73 \pm 0.2$.

3.3. Model verification

Oblique incidence pulse-echo measurements were conducted using a JSR DPR-300 pulser-receiver, an Olympus $f_0 = 5$ MHz focused transducer (3 - inch focal length, 0. 25 - inch element diameter), an ADLink PCIe-9852 DAQ card and a computer-controlled micro-positioning system. The sampling rate for the digitizer was 200MHz. The measurements were conducted in a water tank. In order to increase sensitivity to sub-wavelength flaws, a high gain of 55 dB was used (in which case, grain noise cannot be avoided.). A total of 800 (40 × 20) waveforms were recorded by scanning the microstructure reference region over a rectangular grid of 39 mm × 19mm with a resolution of 1 mm. The separation between any two consecutive positions is sufficient to keep all signals uncorrelated [28].

The extracted mean grain radius and distribution width ($\bar{L} = 13.6$ μm, $\sigma_d = 0.74$)) obtained from the microscopic analysis are used in modified theoretical T-T model to generate Φ_A^{theory}. The result is compared with the experimental spatial variance in Fig. 5. The results show good agreement, which suggests the parameters obtain through microscopic evaluation can be used to determine the upper bound $U(t)$. There is a deviation between the theoretical and experimental curves before the peak (~42 μs). This deviation may be caused by the side-lobes of the sound field, which are ignored in the single Gaussian beam model used here. The surface roughness may also be a contributing factor, as there are still some small scratches on specimen B (see Fig. 3(a)). The deviation from the model after the peak (after 45 μs) may be caused by the assumptions of single scattering, which neglects higher-order scattering effects. The Φ_B^{theory} curve is generated using $\bar{L} = 13.6\ \mu$m without a distribution, resulting in large deviation between the theoretical and experimental curves. This result further demonstrates the importance of including the grain size distribution.

The theoretical maximum amplitudes of grain noise, the bounds and the experimental result from the microstructure reference region are shown in Fig. 6. The experimental spatial correlation coefficient (SCC) [28] is 0.28 ± 0.13 using a time gate from 42.08 to 52.01 μs, such that the data satisfy the independent and identically distributed (IID) condition. From Fig. 6, it can be observed that a higher confidence means more grain noise can be included within the upper bound. However, there are crossings of the threshold for all lower bounds. The experimental spatial variance curve deviates from the theoretical curve at the peak near 44 μs, where a local valley occurs (also seen in Fig. 5). The valley is part of the measured variance curve, such that $A_{\max}^{\exp}(t)$ is crossing below the lower bounds in this region. The reason might be imperfect alignment of the waveforms. Because there are no front-wall or back-wall echoes available for reference, it is difficult to align the waveforms accurately. Another potential cause for this valley may be that the specimen does not completely satisfy the assumption of

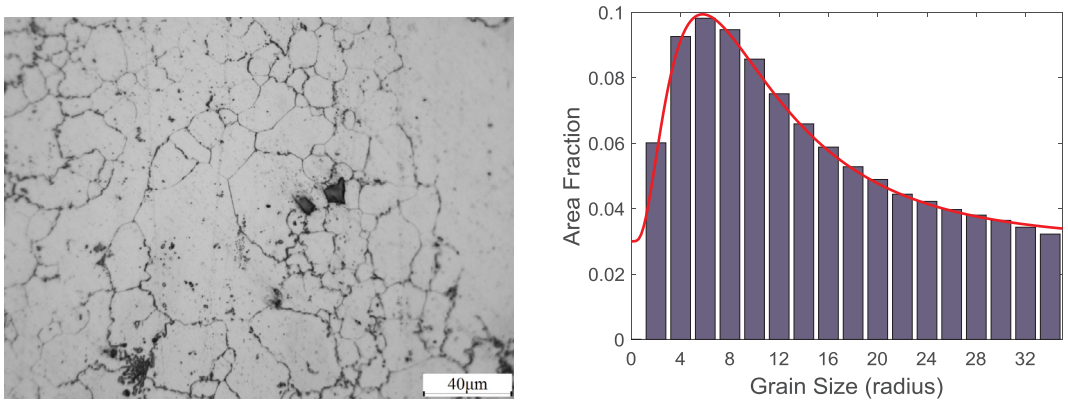

Fig. 4. Microstructure and grain size distribution of AZ80 magnesium alloy (a) metallographic result, (b) grain size distribution with fit shown ($\bar{L} = 13.4 \pm 0.2\,\mu m$, $\sigma_d = 0.73 \pm 0.2$).

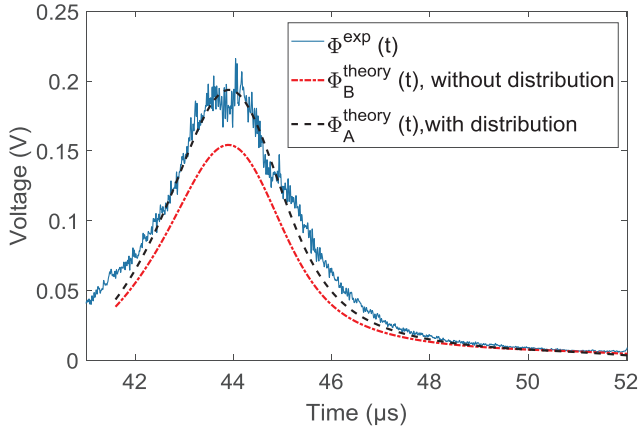

Fig. 5. Experimental variance curve for tests conducted on the AZ80 magnesium alloy using a 5 MHz focused transducer. The theoretical variance curves with distribution and without distribution are also shown.

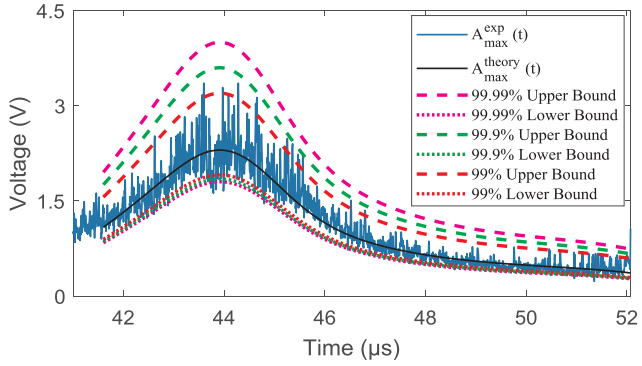

Fig. 6. The maximum amplitudes of grain noise and the effects of confidence level on the bounds (a) with grain size distribution; (b) without grain size distribution.

statistical homogeneity. Fortunately, the effect of this anomaly on flaw detection measurements is negligible.

In short, when the microstructure is known, the theoretical maximum possible grain noise amplitude and the corresponding bounds can be estimated. Then, the present method can be used to inspect sub-wavelength near-surface flaws with a conventional ultrasonic C-scan approach at common frequencies. This topic is described in the next section.

3.4. Ultrasound C-Scan experiment

To highlight the advantage of the proposed method, C-scan experiments were conducted using a normal incidence longitudinal wave method and the oblique incidence transverse wave method proposed in this paper. The experimental parameters are the same as those in the verification experiment. The C-scan images using the longitudinal wave method proposed by Song [13] et al. are shown in Fig. 7(a), which is segmented using a time dependent threshold with 99.9% confidence level. One can see missed detections of SDH A in this case. Note that the background of Fig. 7(a) is clean, showing that false positives can be avoided using a time dependent threshold. However, this method cannot differentiate the flaw echo of SDH A from the dead zone using the effective time gate shown in Fig. 7(b).

The C-scan images based on the transverse wave method are shown in Fig. 8, which are segmented using (a) a fixed threshold of 3.0 V, and (b–c) time dependent threshold without and with consideration of the grain size distribution at 99.9% confidence level, respectively. All four SDHs are clear in the C-scan images, but several false positives exist in Fig. 8(a) and (b). To further illustrate the present method, Fig. 8(d) shows the relationship between the waveforms, the theoretical upper bounds and the time gate. For example, a high grain noise waveform of No.1 region in Fig. 8(a) and (b) will generally treated it as a flaw echo, while the time dependent threshold considering the grain size distribution has better performance for differentiating them and limiting false positives. As the time dependent threshold is concerned, a higher confidence level will lead to lower false positive rate. Additionally, the gain of the pulser-receiver should not be set too high, as the one used for the diffuse ultrasonic backscatter measurement (55 dB was used here). Although a high gain can be beneficial for detection, when the gain is too high, the grain noise will saturate and no longer satisfy the normal distribution.

4. Conclusion

In this article, a new time-dependent threshold method based on a transverse-to-transverse (T-T) scattering model has been applied to detect sub-wavelength near-surface flaws and was shown to have several advantages: (1) After the grain size distribution is introduced to modify T-T model, the near-surface grain noise in ultrasonic transverse wave and its corresponding bounds can be accurately estimated with extreme value theory; (2) The upper bound of grain noise can be treated as a time dependent threshold for C-scan image segmentation of sub-wavelength flaws near the specimen surface; (3) Experimental results show that the present method has good performance for detection of small flaws ($0.305\lambda_T$) and it can suppress both the missed detections and

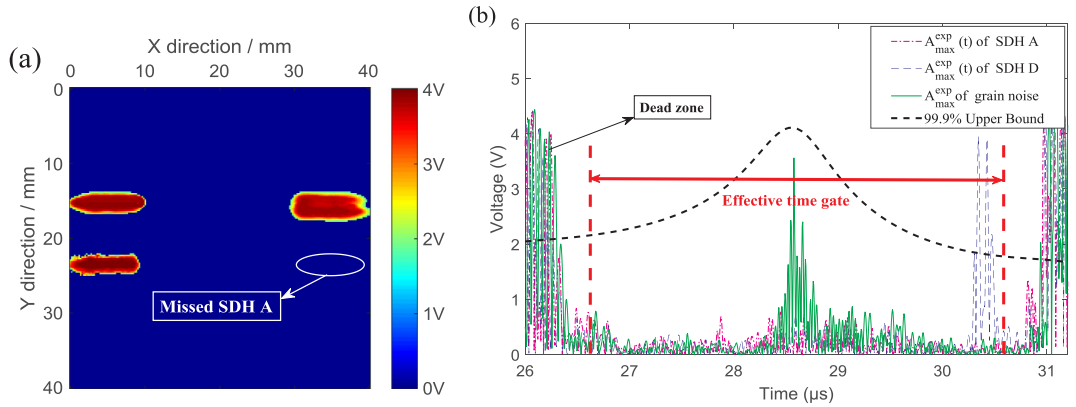

Fig. 7. Ultrasonic testing results using the normal incidence longitudinal wave method (a) the time-dependent threshold with 99.9% confidence level; (b) the relationship between the waveforms, the theoretical upper bound and the time gate;

the false positives. In the future, this work can be extended to strong scattering materials and higher-order scattering, in order to determine when this approach breaks down. The manufacturing and testing of smaller artificial flaws by unconventional machining technology may be needed, but it is still a challenging mission.

Acknowledgement

This work was supported by the National Natural Science Foundation of China [grant numbers 51575541, 51711530231], and the Fundamental Research Funds for the Central Universities of Central South University [grant numbers 2019zzts538]. The authors would like to thank Drs. Ping Hu and Andrea Arguelles for valuable discussions.

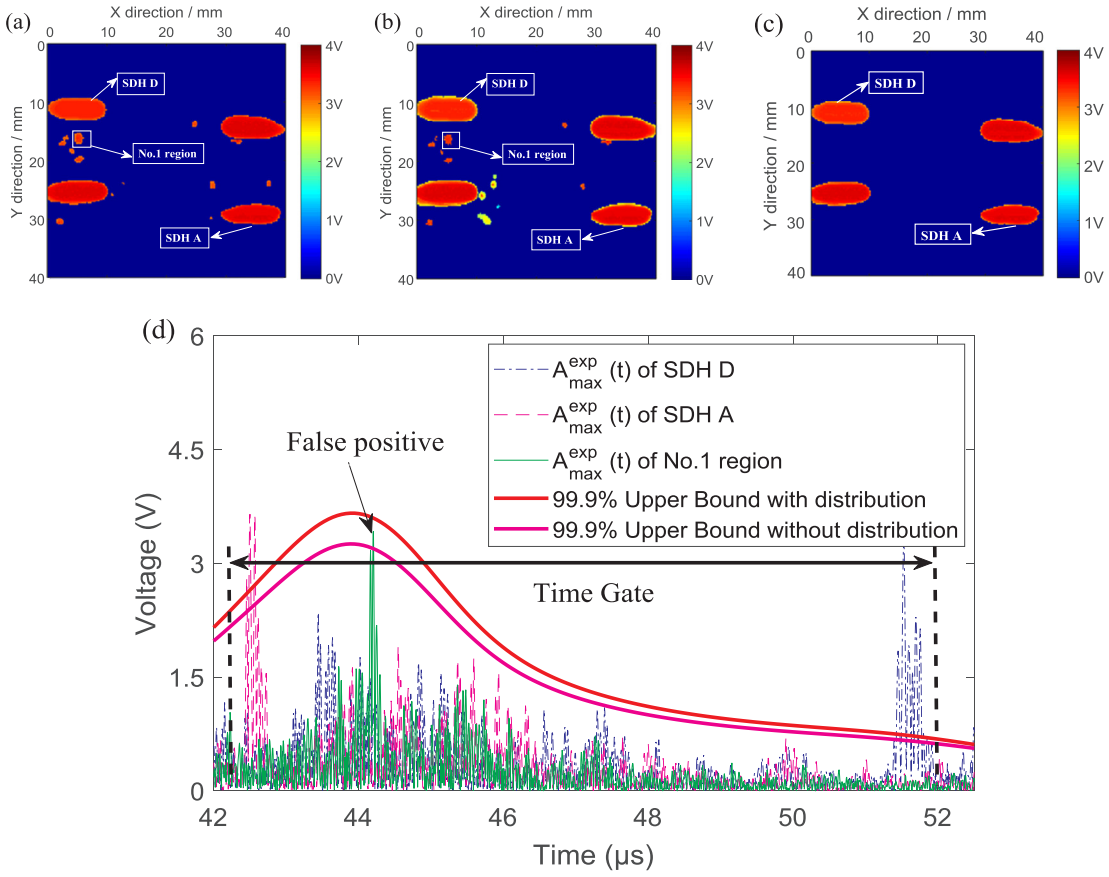

Fig. 8. Ultrasonic testing results using transverse wave method (a) the fixed threshold of 3.0 V; (b) the time-dependent threshold without consideration of the grain size distribution at 99.9% confidence level; (c) the time-dependent threshold with consideration of the grain size distribution at 99.9% confidence level; (d) the relationship between the waveforms, the theoretical upper bound and the time gate.

Appendix A

A.1. The transverse attenuation coefficient

The transverse attenuation coefficient of specimen discussed in Section 2 can be expressed as [18]:

$$\begin{aligned}\alpha_T = {} & \frac{\pi^2\omega^4}{4c_L^5 c_T^3 \rho^2}\int_{-1}^{+1}\widetilde{\eta}_{TL}(\theta_{ps})(M(\theta_{ps}) - L(\theta_{ps}))d\cos\theta_{ps} \\ & + \frac{\pi^2\omega^4}{2c_T^8\rho^2}\int_{-1}^{+1}\widetilde{\eta}_{TT}(\theta_{ps})(N(\theta_{ps}) - 2M(\theta_{ps}) + L(\theta_{ps}))d\cos\theta_{ps},\end{aligned} \tag{A1}$$

where $N_1(\theta_{ps})$, $N_2(\theta_{ps})$, $N_3(\theta_{ps})$ are given as

$$\begin{cases} L(\theta_{ps}) = \Xi_{\cdots\cdots}^{\hat{\mathbf{p}}\hat{\mathbf{p}}\hat{\mathbf{s}}\hat{\mathbf{s}}} = \Xi_{ijkl}^{\alpha\beta\gamma\delta}\hat{p}_\alpha\hat{p}_i\hat{s}_\beta\hat{s}_j\hat{p}_\gamma\hat{p}_k\hat{s}_\delta\hat{s}_l \\ \qquad = \frac{1}{1575}(L_0 + L_1\cos^2\theta_{ps} + L_2\cos^4\theta_{ps}) \\ M(\theta_{ps}) = \Xi_{\cdots\cdots}^{\hat{\mathbf{p}}\hat{\mathbf{p}}\hat{\mathbf{s}}}\mathrm{I} = \Xi_{\cdots\cdots}\mathrm{I}_{\hat{\mathbf{p}}\hat{\mathbf{s}}\hat{\mathbf{s}}}^{\hat{\mathbf{s}}\hat{\mathbf{s}}} = \Xi_{ijkl}^{\alpha\beta\gamma\delta}\hat{p}_\alpha\hat{p}_i\hat{s}_\beta\hat{s}_j\hat{p}_\gamma\hat{p}_k\delta_{\delta l} \\ \qquad = \Xi_{ijkl}^{\alpha\beta\gamma\delta}(\hat{p}_\alpha\hat{p}_i\hat{s}_\beta\hat{s}_j\hat{p}_\gamma\hat{p}_k\hat{s}_\delta\hat{s}_l + \hat{p}_\alpha\hat{p}_i\hat{s}_\beta\hat{s}_j\hat{p}_\gamma\hat{p}_k\hat{s}_{1\delta}\hat{s}_{1l} + \hat{p}_\alpha\hat{p}_i\hat{s}_\beta\hat{s}_j\hat{p}_\gamma\hat{p}_k\hat{s}_{2\delta}\hat{s}_{2l}) \\ \qquad = \frac{1}{1575}(M_0 + M_1\cos^2\theta_{ps}) \\ N(\theta_{ps}) = \Xi_{\cdots\cdots}\mathrm{I}_{\hat{\mathbf{p}}\hat{\mathbf{s}}}^{\hat{\mathbf{p}}\hat{\mathbf{s}}}\mathrm{I} = \Xi_{ijkl}^{\alpha\beta\gamma\delta}\hat{p}_{\alpha i}\hat{p}_i\hat{s}_\beta\hat{s}_j\hat{p}_\gamma\hat{p}_k\delta_{\delta l} \\ \qquad = \Xi_{ijkl}^{\alpha\beta\gamma\delta}(\hat{p}_\alpha\hat{p}_i\hat{s}_\beta\hat{s}_j\hat{p}_\gamma\hat{p}_k\hat{s}_\delta\hat{s}_l + 2\hat{p}_\alpha\hat{p}_i\hat{s}_\beta\hat{s}_j\hat{p}_\gamma\hat{p}_k\hat{s}_{1\delta}\hat{s}_{1l} + 2\hat{p}_\alpha\hat{p}_i\hat{s}_\beta\hat{s}_j\hat{p}_\gamma\hat{p}_k\hat{s}_{2\delta}\hat{s}_{2l} \\ \qquad + \hat{p}_{1\alpha}\hat{p}_{1i}\hat{s}_\beta\hat{s}_j\hat{p}_\gamma\hat{p}_k\hat{s}_{1\delta}\hat{s}_{1l} + \hat{p}_{2\alpha}\hat{p}_{2i}\hat{s}_\beta\hat{s}_j\hat{p}_\gamma\hat{p}_k\hat{s}_{2\delta}\hat{s}_{2l} + 2\hat{p}_{1\alpha}\hat{p}_{1i}\hat{s}_\beta\hat{s}_j\hat{p}_\gamma\hat{p}_k\hat{s}_{2\delta}\hat{s}_{2l}) \\ \qquad = \frac{1}{1575}(N_0 + N_1\cos^2\theta_{ps}) \end{cases} \tag{A2}$$

For crystallites with hexagonal crystallographic symmetry, the constants are [18]:

$$\begin{cases} L_0 = 8c_{11}^2 - 40c_{11}c_{12} + 8c_{11}c_{13} + 16c_{11}c_{33} - 64c_{11}c_{44} + 140c_{12}^2 - 200c_{12}c_{13} - 40c_{12}c_{33} \\ \qquad + 160c_{12}c_{44} + 92c_{13}^2 + 8c_{13}c_{33} - 32c_{13}c_{44} + 8c_{33}^2 - 64c_{33}c_{44} + 128c_{44}^2 \\ L_1 = 112c_{11}^2 + 240c_{11}c_{12} - 248c_{11}c_{13} - 216c_{11}c_{33} - 16c_{11}c_{44} - 280c_{12}^2 + 360c_{12}c_{13} - 40c_{12}c_{33} \\ \qquad - 400c_{12}c_{44} - 92c_{13}^2 + 72c_{13}c_{33} + 352c_{13}c_{44} + 92c_{33}^2 + 64c_{33}c_{44} - 48c_{44}^2 \\ L_2 = 72c_{11}^2 - 200c_{11}c_{12} + 112c_{11}c_{13} - 56c_{11}c_{33} - 176c_{11}c_{44} + 140c_{12}^2 - 160c_{12}c_{13} + 80c_{12}c_{33} \\ \qquad + 240c_{12}c_{44} + 48c_{13}^2 - 48c_{13}c_{33} - 128c_{13}c_{44} + 12c_{33}^2 + 64c_{33}c_{44} + 112c_{44}^2 \\ M_0 = 53c_{11}^2 - 70c_{11}c_{12} - 22c_{11}c_{13} - 14c_{11}c_{33} - 184c_{11}c_{44} + 245c_{12}^2 - 350c_{12}c_{13} - 70c_{12}c_{33} \\ \qquad + 280c_{12}c_{44} + 182c_{13}^2 + 8c_{13}c_{33} + 28c_{13}c_{44} + 38c_{33}^2 - 124c_{33}c_{44} + 308c_{44}^2 \\ M_1 = 219c_{11}^2 + 70c_{11}c_{12} - 186c_{11}c_{13} - 322c_{11}c_{33} - 232c_{11}c_{44} - 245c_{12}^2 + 350c_{12}c_{13} + 70c_{12}c_{33} \\ \qquad - 280c_{12}c_{44} - 84c_{13}^2 + 4c_{13}c_{33} + 364c_{13}c_{44} + 124c_{33}^2 + 148c_{33}c_{44} + 84c_{44}^2 \\ N_0 = 679c_{11}^2/4 - 525c_{11}c_{12}/2 - 14c_{11}c_{13} - 63c_{11}c_{33} - 553c_{11}c_{44} + 1855c_{12}^2/4 - 630c_{12}c_{13} \\ \qquad - 35c_{12}c_{33} + 595c_{12}c_{44} + 364c_{13}^2 - 84c_{13}c_{33} + 196c_{13}c_{44} + 91c_{33}^2 - 238c_{33}c_{44} + 791c_{44}^2 \\ N_1 = 1043c_{11}^2/4 - 238c_{11}c_{12} - 371c_{11}c_{13} - 301c_{11}c_{44} + 175c_{12}c_{11} - 112c_{13}^2 - 28c_{13}c_{33} + 532c_{13}c_{44} \\ \qquad + 490c_{12}c_{13} + 147c_{33}^2 + 154c_{33}c_{44} + 105c_{12}c_{13} + 147c_{44}^2 - 385c_{12}c_{44} - 1365c_{12}^2/4 \end{cases} \tag{A3}$$

Appendix B. Supplementary material

Supplementary data to this article can be found online at https://doi.org/10.1016/j.ultras.2019.05.010.

References

[1] J.A. Collins, Failure of Materials in Mechanical Design: Analysis, Prediction, Prevention, Wiley, New York, 1993.
[2] G. Klien, ultrasonic testing of material, 2014.
[3] C. Fritsch, A. Veca, Detecting small flaws near the interface in pulse-echo, Ultrasonics 42 (2004) 797–801.
[4] X.M. Lu, J.M. Reid, K. Soetanto, L. Weng, V. Genis, Cepstrum technique for multilayer structure characterization (2002) 1571–1574.
[5] R. Drai, F. Sellidj, M. Khelil, A. Benchaala, Elaboration of some signal processing algorithms in ultrasonic techniques: application to materials NDT, Ultrasonics 38 (2000) 503–507.
[6] C.A. Zala, High-resolution inversion of ultrasonic traces, IEEE Trans. Ultrason. Ferroelectr. Freq. Control. 39 (1992) 458–463.
[7] E.E. Hundt, E.A. Trautenberg, Digital processing of ultrasonic data by deconvolution, IEEE Trans. Sonics Ultrason. 27 (1980) 249–252.
[8] V. Ermolov, J. Stor-Pellinen, M. Luukkala, Analog pulse compression system for real-time ultrasonic non-destructive testing, Ultrasonics 34 (1996) 655–660.
[9] R. Al Wardany, J. Rhazi, G. Ballivy, J.L. Gallias, K. Saleh, Use of Rayleigh wave methods to detect near surface concrete damage, J. Chem. Inf. Model. 53 (2013) 1689–1699.
[10] M. Goueygou, O. Abraham, J.F. Lataste, A comparative study of two non-destructive testing methods to assess near-surface mechanical damage in concrete structures, NDT E Int. 41 (2008) 448–456.
[11] A.P. Arguelles, C.M. Kube, P. Hu, J.A. Turner, Mode-converted ultrasonic scattering in polycrystals with elongated grains, J. Acoust. Soc. Am. 140 (2016) 1570–1580.
[12] G. Ghoshal, J.A. Turner, Diffuse ultrasonic backscatter at normal incidence through a curved interface, J. Acoust. Soc. Am. 128 (2010) 3449–3458.
[13] Y. Song, J.A. Turner, Z. Peng, C. Chen, X. Li, Enhanced ultrasonic flaw detection using an ultrahigh gain and time-dependent threshold, IEEE Trans. Ultrason. Ferroelectr. Freq. Control. 65 (2018) 1214–1225.
[14] Y. Song, C.M. Kube, J.A. Turner, X. Li, Statistics associated with the scattering of ultrasound from microstructure, Ultrasonics. 80 (2017) 58–61.
[15] C.W. Anderson, E. Castillo, Extreme Value Theory in Engineering, 2006.
[16] P. Hu, J.A. Turner, Transverse-to-transverse diffuse ultrasonic scattering, J. Acoust. Soc. Am. 142 (2017) 1112–1120.
[17] L. Yang, O.I. Lobkis, S.I. Rokhlin, Explicit model for ultrasonic attenuation in equiaxial hexagonal polycrystalline materials, Ultrasonics 51 (2011) 303–309.
[18] C.M. Kube, J.A. Turner, Acoustic attenuation coefficients for polycrystalline materials containing crystallites of any symmetry class, J. Acoust. Soc. Am. 137 (2015) EL476–EL482.

[19] J.A. Turner, Radiative transfer and multiple scattering of diffuse ultrasound in polycrystalline media, J. Acoust. Soc. Am. 96 (1994) 3675.
[20] H. Du, C. Lonsdale, J. Oliver, B.M. Wilson, J.A. Turner, Evaluation of railroad wheel steel with lamellar duplex microstructures using diffuse ultrasonic backscatter, J. Nondestruct. Eval. 32 (2013) 331–340.
[21] H. Du, J.A. Turner, Ultrasonic attenuation in pearlitic steel, Ultrasonics. 54 (2014) 882–887.
[22] A.P. Arguelles, J.A. Turner, Ultrasonic attenuation of polycrystalline materials with a distribution of grain sizes, J. Acoust. Soc. Am. 141 (2017) 4347–4353.
[23] C.M. Kube, J.A. Turner, Voigt, Reuss, Hill, and self-consistent techniques for modeling ultrasonic scattering 1650 (2015) 926–934.
[24] F.J. Margetan, L. Yu, R.B. Thompson, Computation of grain-noise scattering coefficients for ultrasonic pitch/catch inspections of metals, AIP Conf. Proc. 760 (2005) 1300–1307.
[25] L. Yang, O.I. Lobkis, S.I. Rokhlin, An integrated model for ultrasonic wave propagation and scattering in a polycrystalline medium with elongated hexagonal grains, Wave Motion 49 (2012) 544–560.
[26] T.R. Long, C.S. Smith, Single-crystal elastic constants of magnesium and magnesium alloys, Acta Metall. 5 (1957) 200–207.
[27] L.W. Schmerr, S.-J. Song, F. Simonetti, Ultrasonic Nondestructive Evaluation Systems, 2008.
[28] L. Yu, R.B. Thompson, F.J. Margetan, The spatial correlation of backscattered ultrasonic grain noise: theory and experimental validation, IEEE Trans. Ultrason. Ferroelectr. Freq. Control. 57 (2010) 363–378.